Phase diagram of the Kondo lattice model on the kagome lattice

Shivam Ghosh,[1,*] Patrick O' Brien,[2] Christopher L. Henley,[1] and Michael J. Lawler[2]
[1]*Laboratory of Atomic And Solid State Physics, Cornell University, Ithaca, New York 14853, USA*
[2]*Department of Physics, Binghamton University, Binghamton, New York, USA*
(Received 12 September 2015; published 4 January 2016)

We consider the potential for novel forms of magnetism arising from the subtle interplay between electrons and spins in the underscreened kagome Kondo lattice model. At weak coupling, we show that incommensurate noncoplanar multiwave vector magnetic orders arise at nearly all fillings and that this results from Fermi surface effects that introduce competing interactions between the spins. At strong coupling, we find that such a complex order survives near half filling despite the presence of ferromagnetism at all other fillings. We show this arises due to state selection among a massive degeneracy of states at infinite coupling. Finally, we show that at intermediate filling only commensurate orders seem to survive, but these orders still include noncoplanar magnetism. So, the mere presence of both local moments and itinerant electrons enables complex orders to form unlike any currently observed in kagome materials.

DOI: 10.1103/PhysRevB.93.024401

I. INTRODUCTION

Two paths are known whereby local Hamiltonians in lattice models can stabilize complex spin order, meaning both that the spin configurations are complex in space and that the phase diagram contains a zoo of different phases. One well-known path to such complexity is *state frustration*, meaning the ground states are massively degenerate. Any small perturbation, such as disorder [1], dipolar interactions [2], or simply the intrinsic quantum or thermal fluctuations [3–5], then suffices to select a particular state as the unique ground state.

A second path to complexity is through *frustrated interactions*, i.e., there are multiple kinds of Heisenberg spin couplings that cannot be satisfied simultaneously. Complexity may be realized with as few as *two* isotropic neighbor distances but only when the spin sites form a *non-Bravais* lattice, such as kagome or pyrochlore lattices or when the interactions are nonquadratic [6–8]: Rigorously, on Bravais lattices with isotropic Heisenberg quadratic couplings, at most simple coplanar spin spirals are realized [9].

Stable *noncoplanar* complex spin states are particularly intriguing for their unusual rigid-body-like order parameters. They are also motivated experimentally as they realize an anomalous Hall effect due to Berry phases [10–13] and theoretically since if such a phase loses long range order at sufficiently small spin length, it is expected to become a *chiral spin liquid*, induced without any spin-orbit effects [14].

Even more complex behavior is possible when the frustrated spin-spin interactions decay slowly with distance. That is easily realized by coupling local moments to a band of *fermions*, which mediate oscillating couplings between the local Heisenberg moments—the so-called Kondo lattice model (KLM) [8,12,13,15–17].

In this paper, we show that at weak coupling, the kagome KLM supports incommensurate, noncoplanar, multiwave vector spin ordering. These spin orders motivated us to seek the stability of noncoplanar incommensurate phases at intermediate and strong coupling and understand the potential for such novel magnetism to be discovered in materials. We show, by extending recipes to identify and classify states laid out previously [18], that these novel complex orders arise from competing interactions introduced by the fermions near their Fermi surface. It therefore appears to be a weak coupling phenomena. At strong coupling, however, we discover such complex phases survive near half filling due to a separate mechanism: state selection from a massive degeneracy of states at infinite coupling. We then turn to intermediate coupling and find that dominantly commensurate orders appear to survive. But even here, some of the orders are noncoplanar so that at any coupling, complex orders beyond any form currently observed in kagome materials are possible.

II. COMPLEX ORDERS AT WEAK COUPLING

We adopt the KLM Hamiltonian given by

$$\mathcal{H}_{\mathrm{KLM}} = -t \sum_{\langle ij\rangle,\alpha,\beta,\sigma} c^{\dagger}_{i(\alpha)\sigma} c_{j(\beta)\sigma} - J_K \sum_{i=1,\alpha}^{N} \mathbf{S}_{i(\alpha)} \cdot \boldsymbol{s}_{i(\alpha)}. \quad (1)$$

The first term is nearest-neighbor hopping with amplitude t of a single band of noninteracting electrons, with creation operator $c^{\dagger}_{i(\alpha)\sigma}$ at unit cell i and sublattice α. The second term is the Kondo coupling, with $\boldsymbol{s}_{i(\alpha)}$ being the electron spin and $\mathbf{S}_{i(\alpha)}$ being classical Heisenberg spins representing the local moments. We seek the ground state configuration of the local moments $\{\mathbf{S}^{\mathrm{opt}}_{i(\alpha)}\}$ for every fermion filling n and the ratio of the Kondo coupling to the hopping amplitude J_K/t on the premise that we will find complex orders and a complex phase diagram.

Previous methods for finding $\{\mathbf{S}^{\mathrm{opt}}_{i(\alpha)}\}$ were either variational Monte Carlo (MC), with costly fermionic diagonalization at each MC step (this has been recently overcome by an efficient algorithm [16,17]), or were limited to finding optimal states within a subset of commensurate orders with small unit cells [13]. We instead will study the limits $J_K/t \ll 1$ and $J_K/t \gg 1$ perturbatively. This allows access to large system sizes even with incommensurate orders. We begin here with the $J_K/t \ll 1$ limit but will see that extending it with the variational approach will motivate a study of the opposite limit. The effective Hamiltonian in the $J_K/t \ll 1$ regime is

*sg654@cornell.edu

of the form:

$$\mathcal{H}_{\text{eff}} = \frac{1}{2}\sum_{i(\alpha),j(\beta)} J_{i(\alpha)j(\beta)}\mathbf{S}_{i(\alpha)}\cdot\mathbf{S}_{j(\beta)} \tag{2}$$

$$+\frac{1}{4!}\sum_{i(\alpha),\ldots,l(\delta)} K_{i(\alpha),j(\beta),k(\gamma),l(\delta))}\mathbf{S}_{i(\alpha)}\cdot\mathbf{S}_{j(\beta)}\mathbf{S}_{k(\gamma)}\cdot\mathbf{S}_{l(\delta)}$$

$$+\ldots. \tag{3}$$

In the limit $J_K \to 0$ we need only focus on the first term with the RKKY couplings $J_{i(\alpha)j(\beta)}$. To compute these couplings at $T = 0$, we take a grid in reciprocal space; the corresponding real space lattice sizes were up to $N = 3 \times 36^2$. We first locate the Fermi surface corresponding to the chosen filling, then numerically evaluate the usual analytic formula for $J_{i(\alpha)j(\beta)}$ from second-order perturbation theory [8]. Details of the calculation are outlined in Appendix A.

It is well known that RKKY interactions introduce frustrated interactions among the spins [19–21]. The $J_{i(\alpha)j(\beta)}$ here are no different in principle, but the degree of this frustration, shown in the low temperature spin order $\{\mathbf{S}^{\text{opt}}_{i(\alpha)}\}$ obtained from zero and finite temperature Monte Carlo (MC), is striking. For example, at $n = 0.325$, near 1/3 filling, we find a twisted $\sqrt{3}\times\sqrt{3}$ state with an incommensurate wave vector and slight noncoplanarity. This state smoothly evolves to the coplanar $\sqrt{3}\times\sqrt{3}$ order at $n = 1/3$. As n approaches $n = 5/12$, we find the "Cuboc1" [14] state that is commensurate but noncoplanar with 12 different spins in its unit cell all pointing to the edges of a cube. But these are among the simplest states we found. At $n = 0.488$, for example, we found a three wave vector, incommensurate, and noncoplanar state.

To draw these conclusions, we have plotted the optimal MC spin configurations $\{\mathbf{S}^{\text{opt}}_{i(\alpha)}\}$, with the tail of each spin vector at a common origin [18] as shown in Fig. 1. The common origin plot of the "Cuboc1" state is shown in Fig. 1(a) and has a cuboctahedral structure. Similarly, the coplanar nature of the twisted $\sqrt{3}\times\sqrt{3}$ state is readily apparent as shown in Fig. 1(b), where all spins are almost (ignoring the slight width of the coplanar band) coplanar lying in a plane in spin space. However, the complex state at $n = 0.488$ would appear nearly incomprehensible in a common origin plot, having spins that point in nearly all directions.

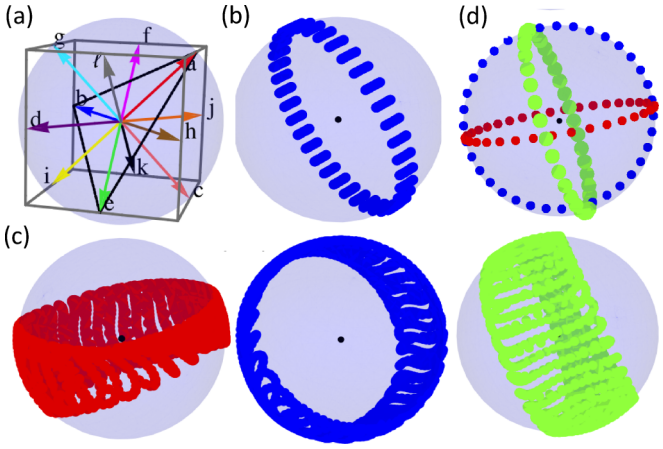

FIG. 1. Some ground state spin orders of the kagome Kondo model at small J_K/t. (a) The "Cuboc1" state [22], found at $n = 5/12$, consisting of 12 different spins pointing to the edges of a cube. (b) An incommensurate twisted $\sqrt{3}\times\sqrt{3}$ state found at $n = 0.325$. (c) Sublattice separated common origin plots of a complex state found at $n = 0.488$ on an $N = 3\times 36^2$ cluster. (d) A simplified version of the three common origin plots presented in (c) emphasizing the 90° rotational symmetry of the respective planes.

To simplify such a complicated pattern of spin order in spin space we resort to a simple method. We construct three independent common-origin plots of spins belonging to each kagome sublattice. These plots, as shown in Fig. 1(c), reveal a different dominant plane for spins belonging to each of the three sublattices. To simplify the spin order even further we look at the spin structure factor, which reveals the Fourier space composition of the order.

The sublattice dependent spin structure factor is given by:

$$\eta_\alpha(\mathbf{q}) = \frac{|\mathbf{S}^{\text{opt}}_\alpha(\mathbf{q})|^2}{\sum_{\mathbf{q}\in 1\text{stB.Z.}}|\mathbf{S}^{\text{opt}}_\alpha(\mathbf{q})|^2}. \tag{4}$$

Here $\mathbf{S}^{\text{opt}}_\alpha(\mathbf{q})$ is the Fourier transform of $\{\mathbf{S}^{\text{opt}}_{i(\alpha)}\}$, $\{\mathbf{S}^{\text{opt}}_{i(\alpha)}\}$ being the optimal spin configuration recovered from numerical MC simulations. The summation in the denominator of Eq. (4) is over the set of reciprocal lattice wave vectors $\{\mathbf{q}\}$ belonging to the kagome first Brillouin zone. For a generic incommensurate order, $\eta_\alpha(\mathbf{q})$ will have most of its weight (typically more than 90%) on a star of six- or twelvefold symmetry related "dominant" wave vectors in the zone. Its remaining weight will lie on other "subdominant" wave vectors which are required for unit spin normalization of the set of spins in real space. For example, the twisted $\sqrt{3}\times\sqrt{3}$ state was found to have a wave vector near the Brillouin zone corner (the $\mathbf{K}$ point) that accounted for 96% of the weight of $\eta_\alpha(\mathbf{q})$ in the zone. Also, all three sublattices had this same dominant wave vector lying near the zone corner. Similarly, each sublattice of the incommensurate state found at $n = 0.488$ had a different dominant wave vector, which accounted for ∼91% of the weight of $\eta_\alpha(\mathbf{q})$ in the zone. Additionally, all three wave vectors were related by $2\pi/6$ rotations. In contrast, for a commensurate order like the $\sqrt{3}\times\sqrt{3}$ state found at $n = 1/3$, the dominant wave vector lying exactly at the zone corner carried the *entire* weight of $\eta_\alpha(\mathbf{q})$ in the zone.

The dominant wave vectors, identified from the structure factor $\eta_\alpha(\mathbf{q})$, can also be used to reconstruct a "purified" spin configuration (see Appendix B). A purified configuration is created by carrying out an inverse Fourier transform of the Fourier amplitudes corresponding to *only* the set of dominant wave vectors. The Fourier space amplitudes corresponding to all the subdominant modes are set to zero. The resulting set of vectors in real space is then normalized by brute force to create a spin configuration that satisfies the constraint of unit spin normalization at every site on the lattice. This prescription of creating a purified spin configuration made out of only the dominant star of wave vectors from the zone is particularly useful in cases of noncoplanar incommensurate orders like the spin state at $n = 0.488$ in Fig. 1(c), where identification of an underlying symmetry in spin space is not clearly observable in the arrangement of spins in real space or even in their common-origin plots. For example, carrying out this prescription for the three wave-vector spin order at $n = 0.488$ reveals the simple

and beautiful symmetry between spins on the three sublattices. Spins on each sublattice trace out coplanar spirals in mutually orthogonal planes, as shown in the common-origin plot of the purified configuration in Fig. 1(d). The main features of the spin orders are thus revealed via the profile of the structure factor in Eq. (4) and the common origin plots.

III. LUTTINGER-TISZA AND THE FERMI SURFACE

To understand how the competing interactions drive the wave vector composition, sublattice dependence, incommensurate order, and noncoplanarity, we have carried out a Luttinger-Tisza (L.T.) analysis [23]. The method begins by diagonalizing $J_{\alpha\beta}(\mathbf{q})$, the spatial Fourier transform of the real space RKKY interactions $J_{i(\alpha),j(\beta)}$:

$$J_{\alpha\beta}(\mathbf{q})u^{\nu}_{\beta}(\mathbf{q}) = \lambda^{\nu}(\mathbf{q})u^{\nu}_{\alpha}(\mathbf{q}), \tag{5}$$

where the ν index labels the three bands in the sublattice space and $\lambda^{\nu}(\mathbf{q})$ is the eigenvalue corresponding to the eigenstate $u^{\nu}(\mathbf{q})$. Then we determine the symmetry related wave vectors $\{\mathbf{Q}_{\text{L.T.}}\}$ with the lowest eigenvalues of $J_{\alpha\beta}(\mathbf{q})$ and the corresponding eigenmodes $u^{\nu}(\mathbf{Q})_{\text{L.T.}}$. The set of Luttinger-Tisza (L.T.) wave vectors $\{\mathbf{Q}_{\text{L.T.}}\}$, along with the corresponding L.T. modes $u^{\nu}(\mathbf{Q})_{\text{L.T.}}$, predict the nature of spin orders stabilized by the RKKY Hamiltonian in Eq. (3) as a function of the electronic filling n.

Before we move on to the L.T. results, to get a sense of the kind of spin orders we might find, we have plotted the first five couplings as a function of filling in Fig. 2. Here, negative (positive) couplings correspond to ferromagnetic (antiferromagnetic) interactions. Clearly, at $n = 0$ we should find ferromagnetism. For $n \lesssim 0.2$ we find a dominant ferromagnetic J_1 coupling and small J_2, J_3, J_{3h}, and J_4 couplings. This suggests the ferromagnetic state should become a spiral. Near $n = 1/3$ we expect a $\sqrt{3} \times \sqrt{3}$ coplanar state known to exist [24] at positive J_1, with small positive J_3, J_{3h}. A similar

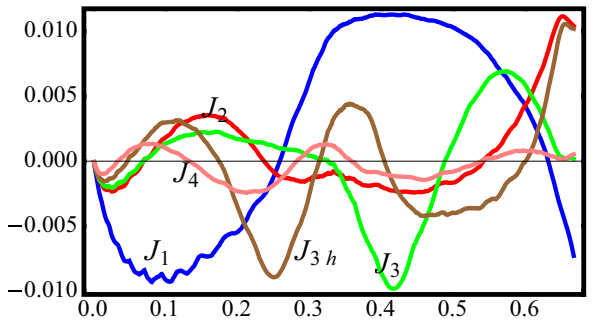

FIG. 2. The first five dominant RKKY couplings on the kagome lattice. The nearest J_1, next nearest J_2, two third nearest J_3, J_{3h} (linking diametrically opposite vertices), and fourth nearest J_4 neighbor couplings plotted as a function of filling n. Positive (negative) couplings correspond to antiferromagnetic (ferromagnetic) interactions. Two notable features of the plot are: oscillations in the sign of the couplings with changing filling n, which leads to frustrated interactions, and intervals of filling where J_1 is not the most dominant interaction. The scale on the y axis is in units of J_K^2/t. The flat kagome band corresponding to fillings from $2/3 < n < 1$ is not part of the analysis.

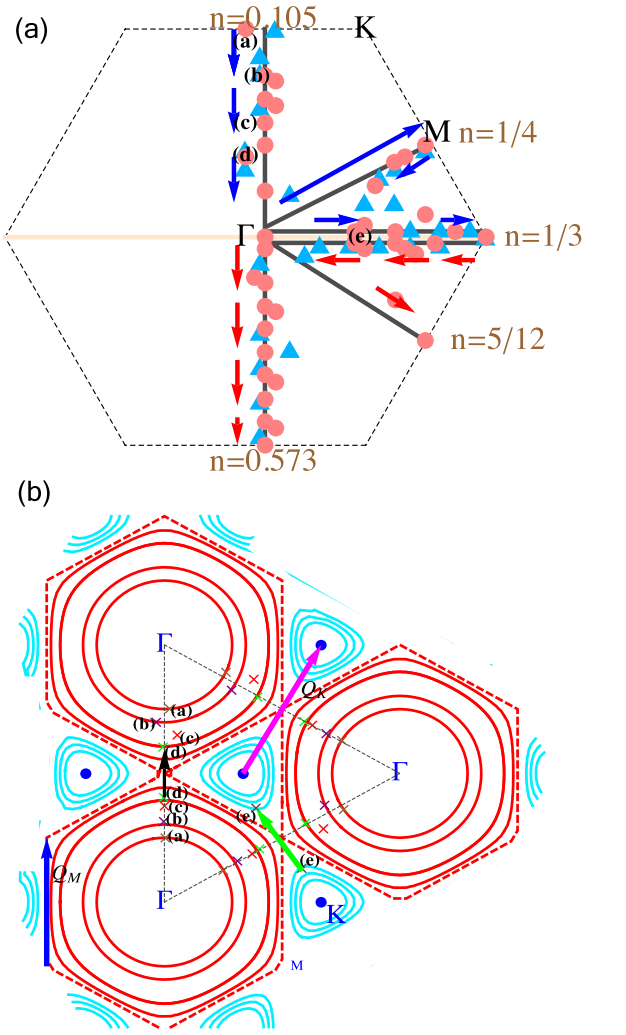

FIG. 3. Luttinger Tisza analysis of the couplings $J_{i(\alpha),j(\beta)}$. (a) The trajectory of the predicted ordering wave vector $\mathbf{Q}_{\text{L.T.}}(n)$ as n is varied for lattice sizes $N = 3 \times 24^2$ (triangles) and $N = 3 \times 36^2$ (circles). Small blue and red arrows indicate the direction of the trajectory of optimal L.T. wave vectors. The large blue arrow shows a first order transition from the zone center to the zone midpoint. (b) Comparison between $\mathbf{Q}_{\text{L.T.}}$ and the Fermi surface. Red contours show $0 < n < 1/4$, dashed red line is the F.S. at $n = 1/4$, and blue contours show $1/4 < n < 1/3$. Several $\mathbf{Q}_{\text{L.T.}}(n)$ are labeled as arrows. Labels (a)–(e) indicate pairs of representative points on the F.S. at different fillings. The black arrow is near $n = 0.488 = 2/3 - 0.179$, the blue arrow is at $n = 5/12$, where $\mathbf{Q}_{\text{L.T.}}(n) = \mathbf{Q}_M$, the green arrow is near $n = 0.325$, and the arrow in pink is at $n = 1/3$, where $\mathbf{Q}_{\text{L.T.}}(1/3) = \mathbf{Q}_K$.

argument leads to the $q = 0$ state near $n = 0.5$. However, at all other fillings simple arguments such as these are not enough to estimate what state will minimize the energy of the RKKY Hamiltonian in Eq. (3).

Plotting the optimal L.T. wave vectors $\mathbf{Q}_{\text{L.T.}}$, as shown in Fig. 3(a), reveals that indeed the predictions from the L.T. method are more complex. The wave vectors do begin at the $\mathbf{Q}_\Gamma = 0$ point at $n = 0$, but they then march towards the Brillouin zone boundary at the $\mathbf{M}$ point by $n = 0.105$ and then return to the Γ point as n approaches $1/4$. This to and fro

march, shown by the small blue arrows in Fig. 3(a), takes place along a mirror symmetry axis of the zone connecting the zone midpoints. However, exactly at $n = 1/4$, and probably for a small interval on either side of it, $\mathbf{Q}_{\text{L.T.}}(n)$ jumps back to the **M** point—a first order transition [shown by the large blue arrow in Fig. 3(a)]. For $1/4 \lesssim n < 1/3$, the $\mathbf{Q}_{\text{L.T.}}(n)$ resumes moving smoothly from the Γ point but switches trajectory moving along a different symmetry axis (connecting the zone corners) towards the **K** point, reaching it uneventfully at $n = 1/3$. For $1/3 < n < 2/3$ wave vectors are the same as those at $2/3 - n$, and their trajectory as a function of filling from $n = 1/3$ to $n = 1/4$ is shown by the small red arrows. What causes such a flow of the optimal L.T. wave vectors in the zone as a function of the filling?

This complex dance of the wave vector must be related to the evolution of the $J_K = 0$ Fermi surface [25]. To see more specifically how the two are related, we have plotted in Fig. 3(b) several $\mathbf{Q}_{\text{L.T.}}$ on top of this Fermi surface as connecting vectors. These vectors connect representative points on the F.S. labeled (a)–(e). We see from this plot that it is the points of maximum curvature of the surface that determine $\mathbf{Q}_{\text{L.T.}}$. This is true at both $n = 0.325$, where we found the twisted $\sqrt{3} \times \sqrt{3}$ state in MC [the optimal L.T. wave vector is shown in green and connects a pair of points on the F.S. labeled by (e)], and at $n = 0.488 = 2/3 - 0.179$, where we found the multiwave vector state [Figs. 1(c) and 1(d)]. An exception to this rule occurs near $n = 5/12$, where the wave vector nests the flat regions of this Fermi surface and lies at the zone midpoint (labeled **M**), as shown by the blue arrow labeled $\mathbf{Q}_M$ in Fig. 3(b). Here we found the cuboc1 state of Fig. 1(a) in MC. The van Hove singularity at $n = 1/4$ also explains the sudden jump in the wave vector as n approaches this filling. Appendix C contains the profile of the Luttinger-Tisza eigenvalues as a function of the electronic filling for several fillings in the range $1/3 < n < 5/12$. So the wave vector predictions from the L.T. analysis are entirely determined by the geometry of the Fermi surface.

Finally, we look at both $Q_{\text{L.T.}}$ and the eigenmodes $u^{\nu}(\mathbf{Q}_{\text{L.T.}})$ to compare with the MC results. At $n = 1/3$ we find $Q_{\text{L.T.}}$ is at the zone corner **K** point [shown by the vector $\mathbf{Q}_K$ in Fig. 3(b)], which is the wave vector of the $\sqrt{3} \times \sqrt{3}$ state (see Appendix B), and the associated L.T. mode $u^{\nu}(\mathbf{Q}_{\text{L.T.}}) = \sqrt{1/3}(1,1,1)$ has equal weights on all sublattices. Such an equally weighted eigenmode indicates that the corresponding wave vector is being used in a perfectly symmetric manner by all three sublattices in creating the spin configuration. This is in agreement with both the common origin plots and the structure factors $\eta_{\alpha}(\mathbf{Q}_{\text{L.T.}})$ [Eq. (4)]: The profile of $\eta_{\alpha}(\mathbf{Q}_{\text{L.T.}})$ in the zone, obtained from MC simulations, shows sharp peaks at the zone corners [labeled **K** in Fig. 3(b)]. Similarly, at $n = 5/12$, we find the star of L.T. wave vectors to lie at the zone midpoints, labeled M in Fig. 3(b), and the modes are given by: $u^{\nu}(\mathbf{Q}_{\text{L.T.}}) = \sqrt{1/2}(1,1,0)$ [for the other two $\mathbf{Q}_{\text{L.T.}}$, related by $2\pi/3$ rotations, the vectors are $\sqrt{1/2}(1,0,1)$ and $\sqrt{1/2}(0,1,1)$]. This is again exactly what is seen in the structure factor Eq. (4) near $n = 5/12$, where prominent features indicating high Fourier weights begin appearing at the zone midpoints.

At $n = 0.488$ we find $u^{\nu}(\mathbf{Q}_{\text{L.T.}})$ has weight on only one sublattice for a given $\mathbf{Q}_{\text{L.T.}}$, so $u^{\nu}(\mathbf{Q}_{\text{L.T.}}) \approx (1,0,0)$. This observation is again consistent with the profile of the three structure factors $\eta_{\alpha}(\mathbf{Q}_{\text{L.T.}})$, one for each $\alpha = 1,2,3$. Each structure factor shows a peak at a single wave vector in the zone (strictly speaking, the peak occurs at two locations in the zone: at the wave vector and its partner obtained by a reflection in the origin). The resulting spin order at $n = 0.488$ has spins on each of the three sublattices forming (almost) coplanar spirals in mutually orthogonal planes [see Fig. 1(d)], with the pitch of each spiral determined by $Q_{\text{L.T.}}$ (see Appendix B for a complete parametrization of the spin configuration in terms of the L.T. wave vectors). So the L.T. method predicts both the wave vector and sublattice dependence of the spin order $\{\mathbf{S}^{\text{opt}}_{i(\alpha)}\}$ found in MC.

IV. PHASE DIAGRAM

With the knowledge discussed above, it seems like we can now find the phase diagram in the limit $J_K/t \ll 1$. But since Fermi surface geometry dictates ordering wave vectors, every filling n will have a different ground state spin configuration. In group theory language, the spin order $\{\mathbf{S}^{\text{opt}}_{i(\alpha)}\}$ will be built out of different representations of $SO(3) \times G_{\text{kagome}}$, where $SO(3)$ is the classical spin group and G_{kagome} is the kagome space group. So every spin configuration likely belongs to a different phase.

To navigate this issue, here we will adopt a pragmatic approach to depict the phase diagram. We first label a phase by a triplet of symbols that characterize the wave vector dependence of the spin pattern on each of the three sublattices. For example, we label the spin configuration presented in Fig. 1(b), as the (a_1,a_1,a_1) phase. The symbol (a_1,a_1,a_1) means that all three sublattices have the same dominant wave vector $\mathbf{Q}_a = 2\pi(7/24,0) \approx \mathbf{K}$. The subscript 1 denotes that the magnitude of $\eta_{\alpha}(\mathbf{Q}_a)$ is the same on all three sublattices. Thus, spins on all three sublattices have exactly the same dominant wave vector, and the wave-vector's Fourier weight is also the same on all three sublattices. The state at $n = 0.488$ we label as the (a_1,b_1,c_1) phase, because each sublattice has a different wave vector: $\mathbf{Q}_a$, $\mathbf{Q}_b$, $\mathbf{Q}_c$. But these are related by $2\pi/3$ rotations and have equal Fourier weights $[\eta_1(\mathbf{Q}_a) = \eta_2(\mathbf{Q}_b) = \eta_3(\mathbf{Q}_c)]$. These labels coarse grain the phase diagram. Furthermore, two spin configurations belong to the same phase family if they share the same broken symmetries and their labels evolve smoothly with n (see Appendix D). A drawback of this approach is that it does not specify particular phase relationships between the amplitudes of the same wave vector appearing in different sublattices [the measure $\eta_{\alpha}(\mathbf{q})$ is norm-based], nor does it indicate relative phases between different spin components on a given sublattice. These metrics could distinguish two phases we denote with the same label.

Using this approach, we construct the phase diagram in Fig. 4(a) by computing in MC the spin configurations at each filling in the range $0 \leqslant n \leqslant 2/3$ (at $n > 2/3$ we start filling a flat band and the approach fails). This leads to order $N \approx 3 \times 36^2$ different spin configurations (about the number of sites in the lattice), but our labeling approach groups them into eight phases (see Appendices B and D for more details on the classification of phases). We attempt to put spin orders from almost all fillings for a given lattice size, limited only by the degeneracy (usually twelvefold) in the $J_K = 0$ single particle

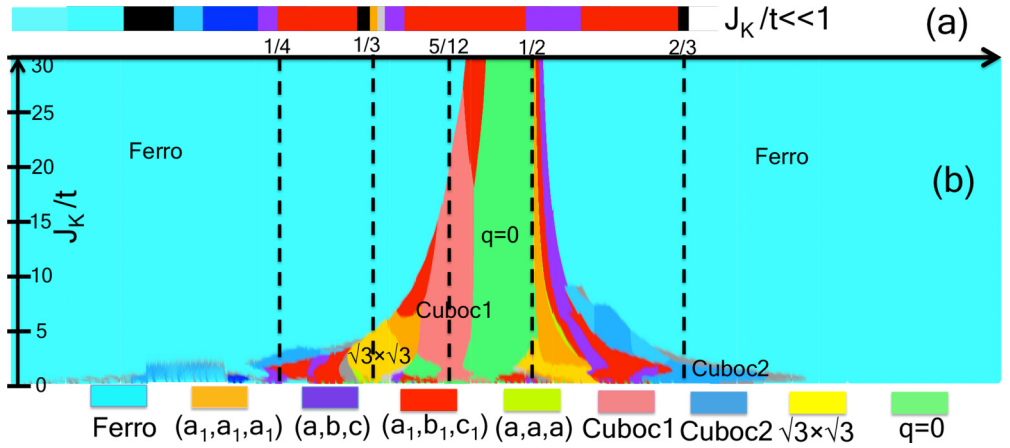

FIG. 4. Phase diagram of the KLM [Eq. (1)]. (a) Exact phase diagram in the limit $J_K/t \ll 1$. Here black regions denote fillings where multiple phases were competitive and our approach could not identify a single dominant phase. (b) Variational phase diagram showing different competing phases at finite J_K/t. The range along the horizontal filling axis is $n = (0,1)$ at unit intervals and along the coupling axis is $J_K = [0.1,10]$ on a grid of 0.05. Energies at every point (n, J_K) in the phase diagram are averaged over 100 values of the boundary phases.

energy levels, where the perturbation approach (Appendix A) fails. The spin orders included in the computation of the phase diagram of Fig. 4(a) include five of the well known commensurate phases: ferromagnetic, cuboc1 [22], cuboc2 [26], the $q = 0$, and $\sqrt{3} \times \sqrt{3}$. The rest are all incommensurate phases recovered from MC simulations (these incommensurate phases are also parametrized based on their symmetries in spin space, see Appendix B).

The $J_K \ll t$ phase diagram in Fig. 4(a) is dominated by noncoplanar incommensurate orders, the most prominent of them being the highly symmetric (a_1,b_1,c_1) phase, shown in red. An example spin configuration from this phase is shown in Figs. 1(c) and 1(d). Commensurate orders, like the $\sqrt{3} \times \sqrt{3}$ order at $n = 1/3$, appear only in tiny slivers. The abundance of incommensurate orders is not surprising since the ordering wave vector(s) of the spin configurations are determined by the geometry of the $J_K = 0$ Fermi surface, which for most fillings does not have a special symmetry (like the Dirac points at $n = 1/3$ and the hexagons at $n = 1/4$ and $n = 5/12$) in the zone.

Given the large database of energetically competitive spin configurations obtained from our numerics, and that the energy of each at finite J_K/t is easily computed, we can also construct a variational phase diagram away from $J_K/t \ll 1$. The result is presented in Fig. 4(b). We see several new features in the phase diagram as J_K/t approaches 1 and larger values. Ferromagnetism begins to dominate much of it above $J_K/t = 1$. The complex ordered states stable at small J_K/t fan out at first but then mostly vanish, and commensurate orders dominate the intermediate J_K/t regime. This provides further evidence that complex orders at small J_K/t resulted primarily from Fermi surface effects. However, there are exceptions to this rule. Some incommensurate orders re-emerge over sizable regions at larger J_K/t especially near $n = 0.5$. The most dominant of these incommensurate orders are the spins belonging to the highly symmetrical (a_1,b_1,c_1) phase. So the phase diagram remains complex at finite J_K/t, but ferromagnetism begins to dominate much of it.

V. STATE SELECTION AT J_K/t

The dominance of ferromagnetism in the phase diagram of Fig. 4 provokes the question of whether there is a threshold value of J_K/t above which it is stabilized at all fillings. To see if this happens, here we consider the $J_K/t \gg 1$ "double-exchange model" regime.

As is well known [27,28], in the $J_K/t \gg 1$ limit, we can switch to coordinates with local quantization axes pointing along the $\vec{S}_{i(\alpha)}$ classical spin directions and find that the energy bands separate into the spin "up" bands and spin "down" bands with a gap proportional to J_K. For $n < 1/2$, we can then integrate out all the higher energy "down" bands and obtain an effective model for the up bands

$$H_{\rm up} = \sum_{\langle i(\alpha), j(\beta)\rangle} t \cos(\theta_{i(\alpha),j(\beta)}/2) e^{i a_{i(\alpha)j(\beta)}} u^{\dagger}_{i(\alpha)} u_{j(\beta)} + \text{H.c.}, \quad (6)$$

where spinless fermion operator $u^{\dagger}_{i(\alpha)}$ creates an "up" spin on site $i(\alpha)$, $\theta_{i(\alpha),j(\beta)}$ is the relative angle between classical spin vectors on the two sites and $a_{i(\alpha)j(\beta)}$ is a vector gauge potential arising from the noncoplanarity of spins [10].

This hopping process then contributes substantially to the energy if the spins are parallel and $\theta_{i(\alpha),j(\beta)} = 0$ but contributes nothing if the spins are antiparallel with $\theta_{i(\alpha),j(\beta)} = \pi$. Hence, in the $J_K/t \gg 1$ regime, ferromagnetism will likely dominate and the complex orders discovered at small J_K/t will vanish. However, this argument fails at $n = 1/2$ since here we completely fill the up bands and hopping costs energy of order $\sim J_K$, and in the limit $J_K \to \infty$, all spin states are energetically degenerate.

To resolve this degeneracy, we have carried out a perturbative calculation to second order in t/J_K at $n = 1/2$. It reveals nothing but the nearest neighbor antiferromagnetic Heisenberg model $J \sum_{\langle i(\alpha),j(\beta)\rangle} \mathbf{S}_{i(\alpha)} \cdot \mathbf{S}_{j(\beta)}$ with $J = t^2/J_K$. So at $n = 1/2$, antiferromagnetic states dominate over the ferromagnetic state even at $J_K/t \to \infty$. On a triangular lattice, such a Hamiltonian would favor the coplanar 120 degree state. However, on non-Bravais lattices like the kagome and

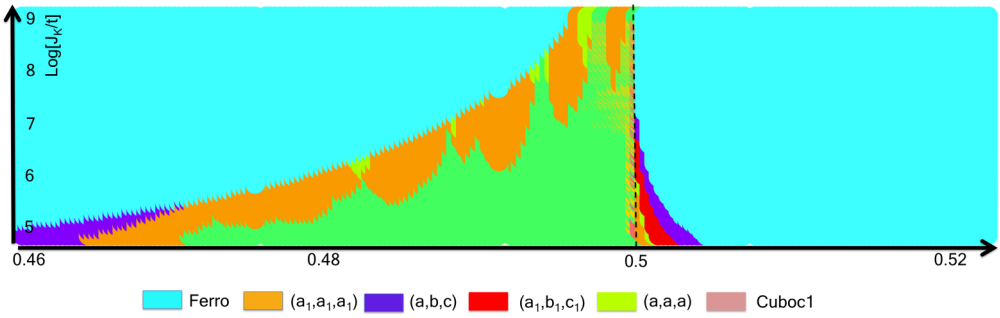

FIG. 5. Variational phase diagram in the large-J_K/t regime. This phase diagram includes 48 states taken from the set of MC ground states at $J_k/t \ll 1$, and the set of commensurate orders consisting of the $q = 0$, $\sqrt{3} \times \sqrt{3}$, cuboc1, cuboc2, and ferromagnetic state.

pyrochlore, the Hamiltonian has no unique ground state and is extensively (scaling with the system size) degenerate.

Achieving a full understanding of the $n \approx 1/2$, large J_K/t regime is therefore a state selection problem on the kagome lattice. In the presence of temperature [5,29] or quantum [24,30] fluctuations, it is known that the $\sqrt{3} \times \sqrt{3}$ state is selected. It seems natural to expect that this state will also appear at $n = 1/2$. However, the fluctuations here favor the cuboc1 state as shown by our variational calculations (Cuboc1 is also selected in a more trivial state selection problem, see Appendix E). It is akin to the state selection through order by disorder by either temperature or quantum fluctuations of the nearest neighbor kagome Heisenberg model. The fluctuations that produce the selection here, however, results from the fermions as they try to hop around in the presence of the spins.

Motivated by this switch from ferromagnetism to antiferromagnetism, we have produced a variational phase diagram in Fig. 5, in the vicinity of $n = 1/2$ up to $J_K/t = 10^4$. We see in this plot that even at these extreme values, the antiferromagnetic state at $n = 1/2$ does not make a direct transition into the ferromagnetic state. Instead, a series of commensurate and incommensurate orders intervene. So, state selection among all possible magnetic states, both ferromagnetic and antiferromagnetic, is responsible for the survival of complex order near $n = 1/2$ and $J_k/t \gg 1$.

VI. CONCLUSION

Our results show that the underscreened Kondo regime supports complex forms of magnetic order with noncoplanar, incommensurate, and multiwave vector properties throughout much of its phase diagram and therefore provides useful insight that can guide the search for such magnetism in materials. To reveal these complex spin orders and to produce the phase diagram in Fig. 4, we approached the Kondo Hamiltonian from several fronts. In Sec. II, we first took the limit $J_K/t \ll 1$ of the Kondo Hamiltonian and derived the RKKY Hamiltonian in Eq. (3): a simple Heisenberg exchange Hamiltonian with long ranged, oscillatory interactions. We solved the RKKY Hamiltonian using several parallel and complementary methods. Brute force zero and finite temperature Monte Carlo minimization of the RKKY Hamiltonian revealed a plethora of noncoplanar spin configurations, some of which were commensurate like in Fig. 1(a). However, at most generic fillings, a common-origin plot visualization of the optimal spin configurations showed the emergence of noncoplanar incommensurate orders as in Figs. 1(c) and 1(d) (also see Appendices B and D).

Given the abundance of these noncoplanar incommensurate orders and the lack of attention given to such orders in previous studies [12,13,31] of the Kondo lattice model, we set about exploring their origin in further detail. Using Luttinger-Tisza and Fermi surface geometry arguments in Sec. III, we showed that the ordering wave vectors of the spin configurations were the nesting wave vectors of the Fermi surface (Fig. 3). For most fillings, the nesting wave vectors were incommensurate and connected points on the Fermi surface with the maximal curvature—a mechanism very different from the conventional nesting which connects parallel parts of the Fermi surface at Van-Hove fillings. This nontrivial, yet insightful connection between the Fermi surface geometry and the ordering wave vectors of the spin configurations explained the abundance of incommensurate orders retrieved from MC. Furthermore, the Luttinger-Tisza and Fermi surface nesting arguments show that incommensurate noncoplanar orders will be generic even in other non-Bravais lattices like the pyrochlore, for fillings at which the Fermi surface is not at a special symmetry point in the zone.

Spin configurations retrieved from the RKKY limit were projected variationally to finite values of J_K/t to construct the phase diagram in Fig. 4(b). Not surprisingly, the $J_k/t \ll 1$ parts of the phase diagram showed a plethora of incommensurate phases, some of which were found to survive even at much larger values of J_K/t. The other striking feature of the phase diagram was the dominance of the ferromagnetic order for $J_K/t > 1$.

To explain the dominance of the ferromagnetic order, we approached the Kondo lattice model from the strong coupling limit in Sec. V. In this limit, the effective double exchange Hamiltonian explained the prevalence of the ferromagnetic order at all fillings and large J_K/t except at a half filling, where we found a nontrivial exact degeneracy between *all* spin configurations. This degeneracy is generic to all lattices and is acute in the case of non-Bravais lattices like the kagome and pyrochlore, where it is only partially resolved (to second order in the hopping) in favor of antiferromagnetic orders. Antiferromagnetic orders therefore appear *only* at the special half-filling point in the strong coupling limit of the Kondo lattice model and become more dominant, occupying

increasingly larger parts of the phase diagram, as one moves towards smaller J_K/t values.

It is important to note that the phase diagram in Fig. 4(b) emerged from a simple one band model Eq. (1), and its complexity was uncovered by the variation of two very simple parameters: the electronic filling and the strength of the Kondo coupling relative to the hopping amplitude. Real materials, however, will unlikely be described by the idealized kagome Kondo model we study. Likely, their band structure will be much more complicated, and three dimensionality may be important. The Luttinger-Tisza method, MC calculations at small J_K/t, and hopping model at large J_K/t are easily extended to these cases. Further, additional physics, such as impurities, additional spin-spin interactions, and various magnetic anisotropies can also be handled by these methods. So the methods we establish here will likely play a role in the search and study of complex forms of magnetism arising from under screened Kondo physics.

Finally, we would like to stress that noncoplanar orders appear rarely in kagome systems. Our results suggest that, in Kondo-coupled systems, such as potentially the layered itinerant kagome ferromagnet Fe_3Sn_2 [32] and doped FeCrAs [33] with small spin-orbit effects, noncoplanar commensurate and incommensurate orders are abundant.

Note added. Spin orders discovered in this study and our other results are consistent with a related work [31] on the same model and lattice.

ACKNOWLEDGMENTS

We would like to thank G. W. Chern, C. D. Batista, J. T. Chalker, M. Gingras, I. Martin, and Y. Motome for discussions. C.L.H. and S.G. acknowledge support from NSF Grant NSF DMR-1308089. S.G. was also supported by a Cornell Graduate Fellowship.

APPENDIX A: DERIVATION OF THE RKKY INTERACTIONS

We will derive the RKKY couplings via two different methods in this section and compare results obtained from each method. The first way to get $J_{i(\alpha)j(\beta)}$ is in Fourier space using second order perturbation theory. We define the following electron operators in momentum space:

$$c^{\alpha}_{\mathbf{k}} = \frac{1}{\sqrt{N/3}} \sum_i c_{i(\alpha)} e^{i\mathbf{k}\cdot\mathbf{R}_i}, \tag{A1}$$

where $N/3$ is the number of unit cells and α is the sublattice index. Using Eq. (A1) we first write down the free fermion part of the KLM Hamiltonian in the basis $|\mathbf{k}^{\alpha}\rangle$ as follows,

$$\begin{pmatrix} 0 & -2t\cos(\mathbf{k}\cdot\mathbf{a}_{12}) & -2t\cos(\mathbf{k}\cdot\mathbf{a}_{13}) \\ -2t\cos(\mathbf{k}\cdot\mathbf{a}_{12}) & 0 & -2t\cos(\mathbf{k}\cdot\mathbf{a}_{23}) \\ -2t\cos(\mathbf{k}\cdot\mathbf{a}_{13}) & -2t\cos(\mathbf{k}\cdot\mathbf{a}_{23}) & 0 \end{pmatrix}, \tag{A2}$$

where $\mathbf{a}_{\alpha\beta} = \mathbf{a}_{\alpha} - \mathbf{a}_{\beta}$, $\mathbf{a}1 = (0,0)$, $\mathbf{a}_2 = (1,0)$, and $\mathbf{a}_3 = (1/2, \sqrt{3}/2)$. Both $\mathbf{a}_{2(3)}$ are one half of lattice vectors that define the kagome unit cell. Diagonalizing (A2) yields three bands ν with single particle energies $\varepsilon^{\nu}_{\mathbf{k}}$, eigenvectors $u^{\nu}_{\mathbf{k},\alpha}$, and a new set of operators $c^{\nu\dagger}_{\mathbf{k}} = \sum_{\alpha} u^{\nu}_{\mathbf{k},\alpha} c^{\alpha\dagger}_{\mathbf{k}}$. We can now look at the Kondo perturbation to the free fermion dispersion.

The Kondo part of Eq. (1) in this paper can be expressed in real space as

$$\begin{aligned} \mathcal{H}_{\text{Kondo}} = -\frac{J_K}{2} \sum_i \sum_{\alpha} (& S^{-}_{i(\alpha)} c^{\dagger}_{i(\alpha)\uparrow} c_{i(\alpha)\downarrow} \\ & + S^{+}_{i(\alpha)} c^{\dagger}_{i(\alpha)\downarrow} c_{i(\alpha)\uparrow} + S^{z}_{i(\alpha)} c^{\dagger}_{i(\alpha)\uparrow} c_{i(\alpha)\uparrow} \\ & - S^{z}_{i(\alpha)} c^{\dagger}_{i(\alpha)\downarrow} c_{i(\alpha)\downarrow}). \end{aligned} \tag{A3}$$

Second order perturbation theory will carry two copies of (A3), each of them sandwiched between pairs of electronic states inside $|\mathbf{k}^{\nu}_{\text{in}}\rangle$ and outside $\mathbf{k}^{\nu'}_{\text{out}}$, the F.S. given by

$$E_2(n) = J_K^2 \sum_{\mathbf{k}_{\text{in}}, \mathbf{k}_{\text{out}}, \nu, \nu'} \frac{|\langle \mathbf{k}^{\nu}_{\text{in}} | \mathcal{H}_{\text{Kondo}} | \mathbf{k}^{\nu'}_{\text{out}} \rangle|^2}{(\varepsilon^{\nu}_{\mathbf{k}_{\text{in}}} - \varepsilon^{\nu'}_{\mathbf{k}_{\text{out}}})}. \tag{A4}$$

Insertion of (A3) into (A4) produces 16 terms, out of which only four are nonzero due to spin rotational invariance. Each of these four terms have the same contribution and $E_2(n)$, expressed in Fourier space, then becomes

$$E_2(n) = \sum_{\mathbf{q} \in 1st B.Z.} J_{\alpha\beta}(\mathbf{q}) \mathbf{S}_{\alpha}(\mathbf{q}) \cdot \mathbf{S}_{\beta}(-\mathbf{q}), \tag{A5}$$

where $J_{\alpha\beta}(\mathbf{q})$ is a 3×3 matrix in the sublattice basis and is given by

$$J_{\alpha\beta}(\mathbf{q}) = -\frac{J_K^2}{2} \sum_{\mathbf{k}_{\text{in}}, \nu, \nu'} \frac{u^{\nu *}_{\mathbf{k}_{\text{in}},\alpha} u^{\nu'}_{\mathbf{k}_{\text{in}}+\mathbf{q},\alpha} u^{\nu' *}_{\mathbf{k}_{\text{in}}+\mathbf{q},\beta} u^{\nu}_{\mathbf{k}_{\text{in}},\beta}}{\left(\varepsilon^{\nu'}_{\mathbf{k}_{\text{in}}+\mathbf{q}} - \varepsilon^{\nu}_{\mathbf{k}_{\text{in}}}\right)} e^{-i\mathbf{q}\cdot\mathbf{a}_{\alpha\beta}}, \tag{A6}$$

where $u^{\nu}_{\mathbf{q},\alpha}$ is an amplitude for destroying an electron with wave vector $\mathbf{q}$ in band ν and the summation is restricted to states $\mathbf{k}_{\text{in}}$ below the F.S. Note that in going from (A4) to (A6) we have switched dummy momentum indices from $(\mathbf{k}_{\text{in}}, \mathbf{k}_{\text{out}})$ to $\mathbf{k}_{\text{in}}, \mathbf{q}$. Use of zone symmetries (C_6 and mirror reflections) requires us to compute $J_{\alpha\beta}(\mathbf{q})$ for only $1/12$ of the zone. The real space couplings are obtained by inverse Fourier transforming (A6)

$$J_{i(\alpha)j(\beta)} = \sum_{\mathbf{q}} J_{\alpha\beta}(\mathbf{q}) e^{-i\mathbf{q}\cdot\mathbf{R}_{ij}}. \tag{A7}$$

There are two limitations of computing the set of $\{J_{i(\alpha)j(\beta)}\}$ via the method above. First, symmetries in the zone at any

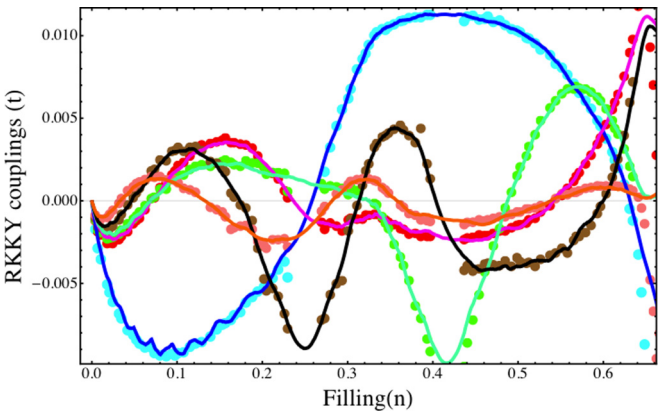

FIG. 6. A comparison of RKKY interactions from two methods: (1) calculation by direct integration in Fourier space, shown via circles, and (2) fitting procedure, shown via lines.

TABLE I. Ordering wave vectors and spin F.T. for reconstructing orders found at $n = 0.321$ and $n = 0.325$. From left to right: filling at which order was found, ordering wave vector $\mathbf{q}$ for the $1\mathbf{Q}(a,a,a)$ state, sublattice phases $\varphi_{2,3}$ [see (B1)] and Norm$\{\mathbf{S}_i^{\text{recons}}\}$.

Filling (n)	$\mathbf{q}(2\pi)$	$\varphi_2(2\pi)$	$\varphi_3(2\pi)$	Norm$\{\mathbf{S}_i^{\text{recons}}\}$
0.321	$\begin{pmatrix}0.27\\0.04\end{pmatrix}$	0.27	2/3	(0.95,0.97)
0.325	$\begin{pmatrix}0.14\\0.29\end{pmatrix}$	0.65	0.27	(0.997,0.998)

filling lead to degeneracies in the single particle energies (typically six leading to twelve missing electronic states) requiring us to "hop" over fillings so as to avoid zero energy denominators in Eq. (A6). The second limitation is a more severe form of the first constraint, where, for a window of fillings near Van Hove points, computation of Eq. (A6) is restricted by large parallel parts of the F.S. with degenerate energies. The first limitation is resolved by averaging (A6) over two nonlocal boundary phases which break the sixfold symmetry to two (associated with spins). To circumvent the second restriction we propose an alternative methodology for computations of $\{J_{i(\alpha)j(\beta)}\}$ as follows.

The second method for extracting the set of couplings is an approach in real space, cruder in spirit, but works as well as the explicit calculation in Fourier space. Using exact numerical diagonalization, we evaluate the single particle energies of fermions in Eq. (1) in this paper in the background of a set of random spin configurations of size N_s for a given J_K. These single particle energies are summed up to the F.S. to find the total energy $E_{ED}(n)$ as a function of filling. Each element from the set of $\{E_{ED}(n)\}$ is fit to the following functional form at different J_K, for all fillings:

$$E_{ED}(n) = E_0^{\text{fit}}(n) + (J_K/t)^2 E_2^{\text{fit}}(n) + (J_K/t)^4 E_4^{\text{fit}}(n) + \ldots, \tag{A8}$$

with fit parameters $\{E_0^{\text{fit}}, E_2^{\text{fit}}, E_4^{\text{fit}}\}$. Once we recover the set of $\{E_2^{\text{fit}}(n)\}$ for all spin configurations in the database, we fit it to the following functional form

$$E_2^{\text{fit}}(n) = \varepsilon_0(n) + J_1^{\text{fit}}(n) \sum_{\langle ij\rangle} \mathbf{S}_i \cdot \mathbf{S}_j + J_2^{\text{fit}}(n) \sum_{\langle\langle ij\rangle\rangle} \mathbf{S}_i \cdot \mathbf{S}_j \tag{A9}$$

TABLE II. Ordering wave vectors and spin F.T. for reconstructing order at $n = 0.311$ occurring in the phase diagram in Fig. 4 in this paper. From left to right: order number corresponding to labeling in Fig. 4 in this paper, ordering wave vector $\mathbf{q}$ for the $1\mathbf{Q}(a,a,a)$ state, spin F.T. at each wave vector. The spin order Fig. 7 has an additional significant contribution (∼30%) on sublattice $\alpha = 1$ from an additional wave vector $\mathbf{q}_2 = 2\pi(0.12,0.19)$ with Fourier weight $\mathbf{S}_{\alpha=1}(\mathbf{q}_2) = (0.25e^{i1.93}, 0.1e^{i1.96}, 0.3e^{-i1.19})$.

$\mathbf{q}(2\pi)$	$\mathbf{S}_1(\mathbf{q})$	$\mathbf{S}_2(\mathbf{q})$	$\mathbf{S}_3(\mathbf{q})$
$\begin{pmatrix}0.12\\-0.19\end{pmatrix}$	$\begin{pmatrix}0.32e^{-i2.9}\\0.4e^{i1.55}\\0.26e^{i2.8}\end{pmatrix}$	$\begin{pmatrix}0.37e^{i0.9}\\0.45e^{-i0.8}\\0.3e^{i0.4}\end{pmatrix}$	$\begin{pmatrix}0.36e^{-i0.5}\\0.43e^{-i2.2}\\0.29e^{-i}\end{pmatrix}$

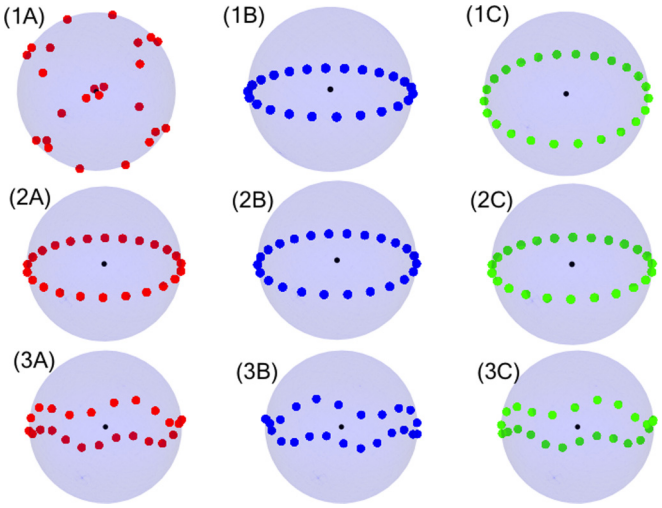

FIG. 7. Common origin plot of incommensurate coplanar spiral orders belonging to (a,a,a) and (a_1,a_1,a_1) phases in Fig. 4 in this paper. 1(A)–1(C): spins on each of the three sublattices for a spin order recovered from MC at $n = 0.311$, 2(A)–2(C): at $n = 0.321$, 3(A)–3(C): at $n = 0.325$. The ordering wave vectors for the three states in Table V and Table II along with Eq. (B1) can be used to construct $\{\mathbf{S}_{i(\alpha)}^{\text{recons}}\}$.

by minimizing the norm of the following matrix equation

$$\underset{J_1^{\text{fit}}(n), J_2^{\text{fit}}(n), \ldots}{\text{Min}} |\mathbf{M}(n) \cdot \mathbf{x}(n) - \mathbf{b}(n)|, \tag{A10}$$

with $\{J_1^{\text{fit}}(n), J_2^{\text{fit}}(n), \ldots\}$ as fit parameters. $\mathbf{M}$ is a $N_s \times (n_J + 1)$, where n_J is the number of couplings to be fit along with an additional constant $\varepsilon_0(n)$ in Eq. (A9). The matrix $\mathbf{M}$ contains the classical energies corresponding to the couplings $J_{1,2,\ldots}(n)$ for each random spin configuration,

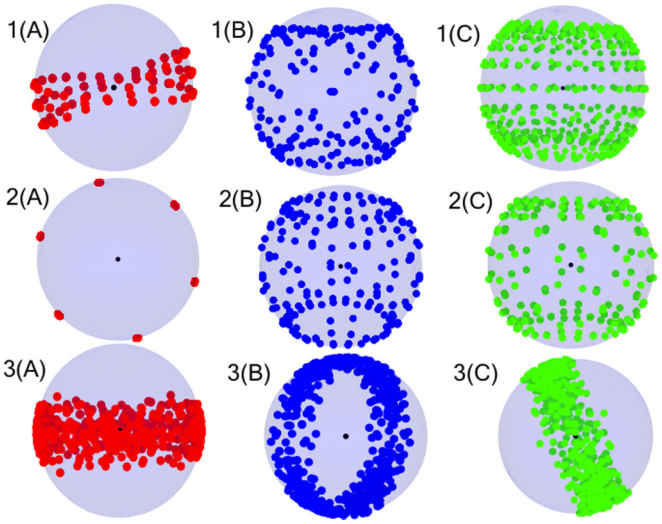

FIG. 8. Common origin plot of spin orders from the (ab,bc,ca) and (a_1b_2,c_1a_2,b_1c_2) phases in Fig. 4 in this paper. 1(A)–1(C): spins on each of the three sublattices for a spin order recovered from MC at $n = 0.115$, 2(A)–2(C): at $n = 0.146$, 3(A)–3(C): at $n = 0.181$. The ordering wave vectors for the three states in Table VIII and $\mathbf{S}_\alpha(\mathbf{q})$ along with (B4) can be used to construct $\{\mathbf{S}_i^{\text{recons}}\}$.

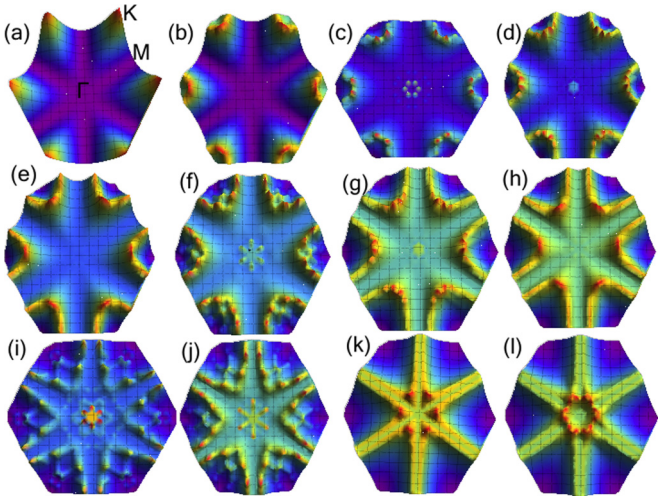

FIG. 9. Eigenvalues $\lambda^{\nu}(\mathbf{q})$ of the $J_{\alpha\beta}(\mathbf{q})$ in the lowest band $\nu = 1$ [see Eq. (3) in this paper] in the kagome first B.Z. (a) 0.333, (b) 0.343, (c) 0.352, (d) 0.354, (e) 0.364, (f) 0.372, (g) 0.375, (h) 0.381, (i) 0.41. Data for $N = 3 \times 36^2$ lattice and color scheme is red (high), blue (low).

arranged along the rows. $\mathbf{x}$ is a vector of length $n_J + 1$ given by $\mathbf{x}^T = (\varepsilon_0(n), J_1(n), J_2(n), \ldots)$, and the vector $\mathbf{b}$ contains the extracted $E_2^{\rm fit}(n)$ from Eq. (A8) for each of the N_s spin configurations.

A comparison of the Fourier and real space methods is shown for the first four RKKY couplings in Fig. 6 as a function of filling n. Both methods have maximum susceptibility to finite size effects at small fillings $n \leqslant 0.1$ and to ferromagnetic background orders where electrons have longer mean free paths comparable to system sizes. We next investigate, in more detail, the various spin orders making up the phase diagram in Fig. 4 in this paper.

APPENDIX B: PARAMETRIZATION OF CLASSICAL SPIN ORDERS

A parametrization of the different spin orders $\{\mathbf{S}_i^{\rm opt}\}$ making up the phases in Fig. 4 in this paper is provided in this section. There are two steps for parametrizing a spin state. In the first step, we construct a purified version $\{\mathbf{S}_{i(\alpha)}^{\rm recons}\}$ of the optimal spin order obtained from MC by filtering out the dominant Fourier modes on each sublattice. In the second step, we try fitting simple functional forms to $\{\mathbf{S}_{i(\alpha)}^{\rm recons}\}$. Since most of the

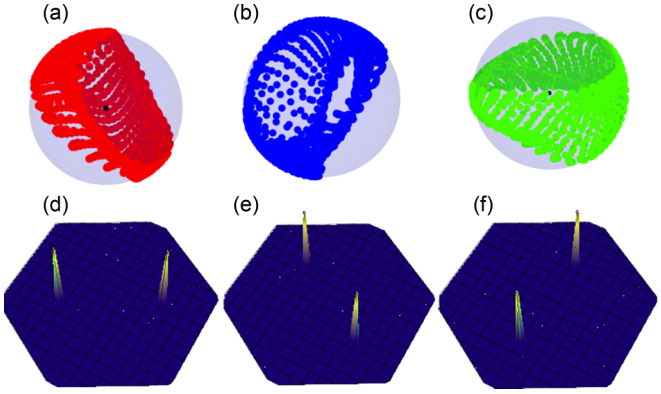

FIG. 10. Common origin plot of spins and the Fourier weights for a spin configuration found at $n = 0.375$ on a $N = 3 \times 36^3$ lattice. (a)–(c) common origin plots showing (a_1,b_1,c_1) phase. (d)–(f) Fourier profile $\eta_\alpha(\mathbf{q})$ [see Eq. (4) in this paper] for $\alpha = 1,2,3$.

states are combinations of simple coplanar incommensurate spirals, we begin by parametrizing coplanar spirals.

A coplanar spiral is parametrized by its ordering wave vector $\mathbf{q}$ and two phases dependent on the locking between the sublattices. For two orthonormal unit vectors $\mathbf{e}_{1,2}$, a coplanar spiral can be parametrized as

$$\mathbf{S}_{i(\alpha)} = \mathbf{Re}[e^{i(\mathbf{q}\cdot\mathbf{R}_i+\varphi_\alpha)}(\mathbf{e}_1 - i\mathbf{e}_2)]. \tag{B1}$$

Depending on the location of $\mathbf{q}$ in the zone, the spiral can further be classified as commensurate (if $\mathbf{q}$ lies at a special symmetry point in the zone) or incommensurate (if $\mathbf{q}$ lies at an arbitrary wave vector). Examples of special commensurate coplanar spirals are the two well known $\mathbf{q} = 0$ and the $\sqrt{3} \times \sqrt{3}$ order with ordering wave vectors $\mathbf{q} = \Gamma$ and $\mathbf{q} = \mathbf{K}$ lying at the zone center and zone corner, respectively. For both orders, $\varphi_\alpha = 2\pi(\alpha - 1)/3$, which makes an angle of $2\pi/3$ between spins, locally, on every triangle. Eq. (B1) can also be used to parameterize incommensurate coplanar spirals, like the states at n = 0.321 and n=0.325, using the parameters in Table I.

An incommensurate order, on the other hand, has a special direction in real space defined by $\mathbf{q}$ and a set of points $\{\mathbf{R}_{i(\alpha)}\}$, such that $\mathbf{q} \cdot \mathbf{R}_{i(\alpha)} = 2\pi m(\sqrt{N/3})^{-1}$ for an integer m. As we move along $\{\mathbf{R}_{i(\alpha)}\}$, we trace out $(\sqrt{N/3})^{-1}$ equally spaced coplanar directions in spin space as shown in Figs. 3(a1)–3(a3) in this paper. An incommensurate coplanar spiral might locally have angles close to $2\pi/3$ as in the twisted $\sqrt{3} \times$

TABLE III. Broken symmetry phases in RKKY limit. Columns from left to right: Filling range n where the phase was found, phase notation (see text), planar or noncoplanar orders, commensurate (CO) or incommensurate (ICO) order, and example spin order.

Filling range	Phase label	Noncoplanar?	CO/ICO	Ex.
(0,0.03)	(a,a,a)	no	CO	FM
(0.115,0.146)	(ab,bc,ca)	yes	ICO	Fig. 8
(0.226,0.25) (0.492,0.551)	(a,b,c)	yes	ICO	Fig. 11
(0.325,0.333)	(a_1,a_1,a_1)	yes	ICO	Fig. 3(a) in this paper
(0.362,0.485) (0.579,0.624)	(a_1,b_1,c_1)	yes	ICO	Fig. 3(b) in this paper

TABLE IV. Dominant wave vectors and their Fourier weights on the sublattices. Left to right: Filling at which the spin order originates in the RKKY limit, dominant wave vectors in the first B.Z., weights of the dominant wave vectors on each of the three sublattices. Fillings 0.115 and 0.146 correspond to (ab,bc,ca) phase, while the more symmetric spin order at 0.181 is a spin set from the (a_1b_2,c_1a_2,b_1c_2) phase. Spin configurations are shown in Fig. 8.

Filling (n)	$\mathbf{q}_1(2\pi)$	$\mathbf{q}_2(2\pi)$	$\mathbf{q}_3(2\pi)$	$\eta_1(\mathbf{q}_1)$	$\eta_1(\mathbf{q}_2)$	$\eta_2(\mathbf{q}_2)$	$\eta_2(\mathbf{q}_3)$	$\eta_3(\mathbf{q}_1)$	$\eta_3(\mathbf{q}_3)$
0.115	$\begin{pmatrix}0.19\\-0.13\end{pmatrix}$	$\begin{pmatrix}0.02\\-0.22\end{pmatrix}$	$\begin{pmatrix}0.20\\0.09\end{pmatrix}$	0.22	0.22	0.28	0.19	0.29	0.19
0.146	$\begin{pmatrix}0.15\\-0.1\end{pmatrix}$	$\begin{pmatrix}0.02\\-0.18\end{pmatrix}$	$\begin{pmatrix}0.15\\-0.1\end{pmatrix}$	0.21	0.21	0.27	0.19	0.28	0.19
0.181	$\begin{pmatrix}0.02\\-0.13\end{pmatrix}$	$\begin{pmatrix}0.1\\0.08\end{pmatrix}$	$\begin{pmatrix}-0.13\\0.05\end{pmatrix}$	0.22	0.22	0.22	0.22	0.22	0.22

$\sqrt{3}$ order—Fig. 3 in this paper and Table V. As discussed in the previous section, the two kinds of spiral orders can belong to an (a,a,a) phase or a more symmetric (a_1,a_1,a_1) phase. States from these phases are shown in Fig. 7 below. Parametrization for state 1(A)-1(C) in Fig. 7 is provided in Table II.

We now consider the more complicated 3**Q** (ab,bc,ca) orders in the phase diagram in Fig. 4 in this paper. The simplest of these orders are the two commensurate *cuboc1* [22] and *cuboc2* [26] orders shown in Fig. 1 in this paper and found at fillings $n = 5/12$ and $n = 2/3$. Each of these orders are made from the three ordering vectors $\mathbf{Q}_{1,2,3} \in \mathbf{M}$ belonging to the

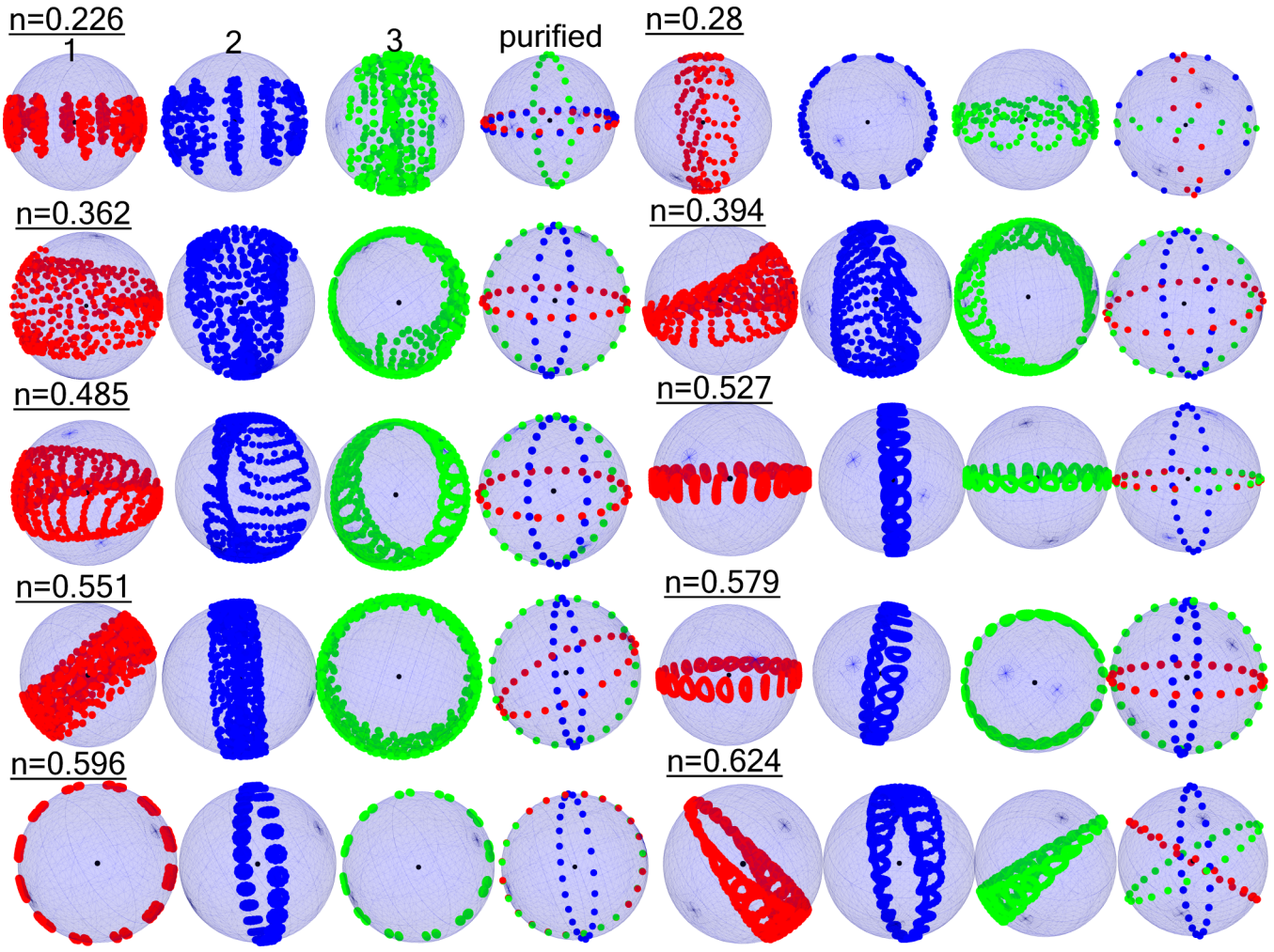

FIG. 11. Common origin plots of the spin configurations from the (a,b,c) and the (a_1,b_1,c_1) phases shown in Fig. 4 in this paper. (A)–(C) label common origin plots for spins on each of the three sublattices, and (D) shows the spins in the "purified" configuration. Also shown and underlined is the filling at which each spin configuration is recovered from MC simulations for a unique set of RKKY interactions, specific to that filling.

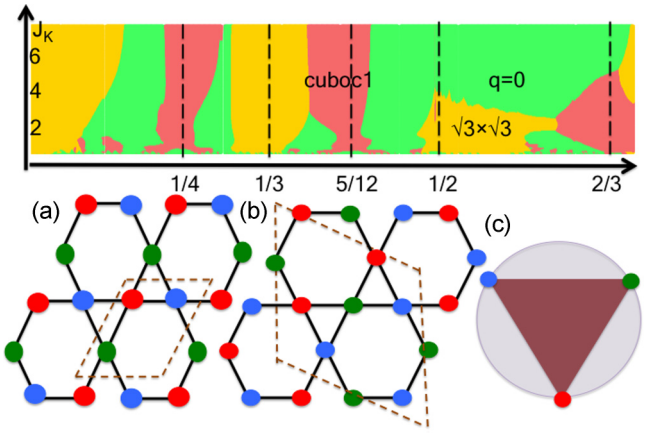

FIG. 12. Variational phase diagram in the presence of a nearest neighbor antiferromagnetic exchange interaction $J_{ex} = 10t$. (a): $\mathbf{q} = 0$, (b): $\sqrt{3} \times \sqrt{3}$, (c): common origin plot of spins for orders in (a),(b).

zone midpoints and leading to a twelve site magnetic unit cell. Each sublattice α uses only two of the three vectors leading to the label $3\mathbf{Q}$ (ab,bc,ca). *Cuboc1* is parametrized as

$$\begin{aligned}
\mathbf{S}_{i(1)} &= \frac{1}{\sqrt{2}}[\cos(\mathbf{Q}_2 \cdot \mathbf{R}_i)\mathbf{e}_2 + \cos(\mathbf{Q}_3 \cdot \mathbf{R}_i)\mathbf{e}_3] \\
\mathbf{S}_{i(2)} &= \frac{1}{\sqrt{2}}[\cos(\mathbf{Q}_1 \cdot \mathbf{R}_i)\mathbf{e}_1 - \cos(\mathbf{Q}_3 \cdot \mathbf{R}_i)\mathbf{e}_3] \qquad \text{(B2)} \\
\mathbf{S}_{i(3)} &= -\frac{1}{\sqrt{2}}[\cos(\mathbf{Q}_1 \cdot \mathbf{R}_i)\mathbf{e}_1 + \cos(\mathbf{Q}_2 \cdot \mathbf{R}_i)\mathbf{e}_2],
\end{aligned}$$

where $\mathbf{Q}_2 = 2\pi(1/4, -1/(4\sqrt{3}))$, $\mathbf{Q}_3 = \mathcal{R}_{\pi/3}\mathbf{Q}_2$, and $\mathbf{Q}_1 = \mathcal{R}_{2\pi/3}\mathbf{Q}_2$. $\mathcal{R}_\theta$ is the 2×2 rotation matrix. The state does not elicit an anomalous Hall response due to the coplanarity of spins on every triangle.

Nearest neighbor spins in the *Cuboc2* state make an angle of $\pi/3$, while the next nearest neighbor spins have an angle of $2\pi/3$ between them. The state is thus favored in the presence of a ferromagnetic J_1 and an AFM J_2 interaction [26]. The noncoplanarity of spins within each triangle in *cuboc2* leads to a nonvanishing value of the scalar spin chirality $\chi = \mathbf{S}_i \cdot (\mathbf{S}_j \times \mathbf{S}_k)$. χ is $+(-)1/\sqrt{2}$ on all the up (down) triangles. The equal and opposite fluxes lead to zero overall flux and no anomalous Hall response. The state has a Z_2 symmetric partner, and at zero temperature, one of the two states is spontaneously selected, breaking Z_2 symmetry. The spin order is parametrized as follows:

$$\begin{aligned}
\mathbf{S}_{i(1)} &= \frac{1}{\sqrt{2}}[\cos(\mathbf{Q}_2 \cdot \mathbf{R}_i)\mathbf{e}_2 + \cos(\mathbf{Q}_3 \cdot \mathbf{R}_i)\mathbf{e}_3] \\
\mathbf{S}_{i(2)} &= \frac{1}{\sqrt{2}}[-\cos(\mathbf{Q}_1 \cdot \mathbf{R}_i)\mathbf{e}_1 + \cos(\mathbf{Q}_3 \cdot \mathbf{R}_i)\mathbf{e}_3] \qquad \text{(B3)} \\
\mathbf{S}_{i(3)} &= \frac{1}{\sqrt{2}}[-\cos(\mathbf{Q}_1 \cdot \mathbf{R}_i)\mathbf{e}_1 + \cos(\mathbf{Q}_2 \cdot \mathbf{R}_i)\mathbf{e}_2].
\end{aligned}$$

TABLE V. Dominant wave vectors and their Fourier weights on the sublattices. Left to right: Filling at which the spin order originates in the RKKY limit, dominant wave vector in the first B.Z., weight of the dominant wave vectors on each of the three sublattices. Spin order at filling 0.321 corresponds to (a,a,a) phase. The more symmetric spin orders found at 0.325 (coplanar spiral Fig. 3 in this paper) and 1/3 ($\sqrt{3} \times \sqrt{3}$ order Fig. 1 in this paper) form part of the (a_1,a_1,a_1) phase.

Filling (n)	$\mathbf{q}(2\pi)$	η_1	η_2	η_3
0.321	$\begin{pmatrix}0.27\\0.04\end{pmatrix}$	0.47	0.47	0.45
0.325	$\begin{pmatrix}0.14\\0.29\end{pmatrix}$	0.497	0.497	0.497
1/3	$\mathbf{K}$	1	1	1

TABLE VI. Set of parameters for constructing the purified spin configurations from the (a,b,c) and (a_1,b_1,c_1) phases according to the ansatz outlined in (B5) for spin configurations shown in Fig. 11.

#	$\mathbf{q}_1(2\pi)$	$\mathbf{q}_2(2\pi)$	$\mathbf{q}_3(2\pi)$	$\varphi_1(2\pi)$	$\varphi_2(2\pi)$	$\varphi_3(2(\pi)$
(6)	$\begin{pmatrix}0.125\\0.12\end{pmatrix}$	$\begin{pmatrix}-0.17\\0.05\end{pmatrix}$	$\begin{pmatrix}0.05\\-0.17\end{pmatrix}$	−0.91	−1.36	−0.86
(12)	$\begin{pmatrix}0.1\\-0.15\end{pmatrix}$	$\begin{pmatrix}0.08\\0.17\end{pmatrix}$	$\begin{pmatrix}0.19\\0.01\end{pmatrix}$	−2.04	−0.58	0.99
(13)	$\begin{pmatrix}0.06\\-0.08\end{pmatrix}$	$\begin{pmatrix}-0.04\\-0.09\end{pmatrix}$	$\begin{pmatrix}0.1\\0.01\end{pmatrix}$	0.39	1.9	1
(14)	$\begin{pmatrix}0.1\\0.08\end{pmatrix}$	$\begin{pmatrix}-0.12\\-0.05\end{pmatrix}$	$\begin{pmatrix}0.02\\-0.13\end{pmatrix}$	0.91	2.26	1.1
(16)	$\begin{pmatrix}0.22\\0.15\end{pmatrix}$	$\begin{pmatrix}0.22\\-0.15\end{pmatrix}$	$\begin{pmatrix}0.02\\0.27\end{pmatrix}$	−0.12	−1.53	−3.02
(17)	$\begin{pmatrix}0.21\\0.1\end{pmatrix}$	$\begin{pmatrix}-0.2\\-0.1\end{pmatrix}$	$\begin{pmatrix}0.02\\-0.23\end{pmatrix}$	−0.48	1.79	−0.97
(18)	$\begin{pmatrix}0.25\\0.12\end{pmatrix}$	$\begin{pmatrix}0.23\\-0.16\end{pmatrix}$	$\begin{pmatrix}-0.02\\-0.28\end{pmatrix}$	1.8	0.64	−0.37
(19)	$\begin{pmatrix}0.22\\0.15\end{pmatrix}$	$\begin{pmatrix}-0.25\\0.12\end{pmatrix}$	$\begin{pmatrix}0.02\\0.27\end{pmatrix}$	0.97	−0.35	0.96

TABLE VII. Dominant wave vectors and their Fourier weights on the sublattices for representative spin orders from the phases (a,b,c) and (a_1,b_1,c_1). Corresponding spin configurations are shown in Fig. 11.

n	$\mathbf{q}_1(2\pi)$	$\mathbf{q}_2(2\pi)$	$\mathbf{q}_3(2\pi)$	$\mathbf{S}_1(\mathbf{q}_1)$	$\mathbf{S}_2(\mathbf{q}_2)$	$\mathbf{S}_3(\mathbf{q}_3)$	$\eta_1(\mathbf{q}_1)$	$\eta_2(\mathbf{q}_2)$	$\eta_3(\mathbf{q}_3)$
0.226	$\begin{pmatrix}0.25\\0.12\end{pmatrix}$	$\begin{pmatrix}-0.25\\0.12\end{pmatrix}$	$\begin{pmatrix}0.02\\-0.27\end{pmatrix}$	$\begin{pmatrix}0.29e^{i1.38}\\0.38e^{i1.48}\\0.48e^{-i0.18}\end{pmatrix}$	$\begin{pmatrix}0.26e^{-i1.82}\\0.38e^{-i1.61}\\0.46e^{i2.95}\end{pmatrix}$	$\begin{pmatrix}0.45e^{i1.48}\\0.39e^{-i0.48}\\0.30e^{i0.29}\end{pmatrix}$	0.92	0.86	0.90
0.341	$\begin{pmatrix}0.12\\-0.24\end{pmatrix}$	$\begin{pmatrix}0.12\\0.24\end{pmatrix}$	$\begin{pmatrix}-0.27\\0.01\end{pmatrix}$	$\begin{pmatrix}0.2e^{-i2.1}\\0.41e^{-i1.36}\\0.2e^{i1.87}\end{pmatrix}$	$\begin{pmatrix}0.49e^{i1.54}\\0.18e^{-i2.5}\\0.14e^{i0.97}\end{pmatrix}$	$\begin{pmatrix}0.06e^{-i1.7}\\0.24e^{i1.44}\\0.47e^{i1.44}\end{pmatrix}$	0.5	0.58	0.57
0.355	$\begin{pmatrix}0.1\\-0.2\end{pmatrix}$	$\begin{pmatrix}0.1\\0.2\end{pmatrix}$	$\begin{pmatrix}-0.23\\0.01\end{pmatrix}$	$\begin{pmatrix}0.18e^{i2.04}\\0.46e^{i1.76}\\0.22e^{-i2.28}\end{pmatrix}$	$\begin{pmatrix}0.42e^{-i0.21}\\0.19e^{-i2.6}\\0.42e^{-i1.7}\end{pmatrix}$	$\begin{pmatrix}0.43e^{-i0.48}\\0.21e^{-i2.88}\\0.44e^{-i1.94}\end{pmatrix}$	0.6	0.8	0.84
0.492	$\begin{pmatrix}0.1\\0.13\end{pmatrix}$	$\begin{pmatrix}0.1\\-0.13\end{pmatrix}$	$\begin{pmatrix}0.06\\0.16\end{pmatrix}$	$\begin{pmatrix}0.27e^{i0.94}\\0.43e^{i1.48}\\0.47e^{-i0.26}\end{pmatrix}$	$\begin{pmatrix}0.45e^{-i3.02}\\0.28e^{i}\\0.43e^{i1.84}\end{pmatrix}$	$\begin{pmatrix}0.27e^{-i2.05}\\0.41e^{-i2.55}\\0.46e^{-i0.81}\end{pmatrix}$	0.96	0.92	0.92
0.527	$\begin{pmatrix}0.23\\0.16\end{pmatrix}$	$\begin{pmatrix}0.23\\-0.15\end{pmatrix}$	$\begin{pmatrix}0.02\\0.27\end{pmatrix}$	$\begin{pmatrix}0.47e^{i1.98}\\0.48e^{i0.3}\\0.2e^{i1.23}\end{pmatrix}$	$\begin{pmatrix}0.47e^{-i1.87}\\0.17e^{-i2.55}\\0.49e^{-i0.34}\end{pmatrix}$	$\begin{pmatrix}0.46e^{-i1.98}\\0.47e^{-i0.3}\\0.21e^{-i1.19}\end{pmatrix}$	0.98	0.98	0.96
0.551	$\begin{pmatrix}0.21\\0.1\end{pmatrix}$	$\begin{pmatrix}-0.2\\0.1\end{pmatrix}$	$\begin{pmatrix}0.02\\-0.22\end{pmatrix}$	$\begin{pmatrix}0.01e^{-i2.17}\\0.49e^{i1.15}\\0.47e^{i2.7}\end{pmatrix}$	$\begin{pmatrix}0.45e^{-i2.86}\\0.49e^{-i1.35}\\0.19e^{i3.10}\end{pmatrix}$	$\begin{pmatrix}0.48e^{i0.39}\\0.03e^{-i2.91}\\0.47e^{i1.98}\end{pmatrix}$	0.92	0.94	0.9
0.28	$\begin{pmatrix}0.125\\0.12\end{pmatrix}$	$\begin{pmatrix}-0.17\\0.04\end{pmatrix}$	$\begin{pmatrix}0.04\\-0.17\end{pmatrix}$	$\begin{pmatrix}0.25e^{-i1.69}\\0.49e^{i3.02}\\0.43e^{-i1.69}\end{pmatrix}$	$\begin{pmatrix}0.41e^{i0.43}\\0.44e^{-i1.47}\\0.35e^{i2.68}\end{pmatrix}$	$\begin{pmatrix}0.48e^{i1.2}\\0.28e^{i2.5}\\0.41e^{i2.9}\end{pmatrix}$	0.96	0.96	0.96
0.362	$\begin{pmatrix}0.1\\-0.15\end{pmatrix}$	$\begin{pmatrix}0.08\\0.16\end{pmatrix}$	$\begin{pmatrix}0.18\\0.01\end{pmatrix}$	$\begin{pmatrix}0.43e^{i0.16}\\0.4e^{-i1.51}\\0.22e^{-i1.06}\end{pmatrix}$	$\begin{pmatrix}0.36e^{-i2.31}\\0.29e^{-i1.76}\\0.42e^{i2.6}\end{pmatrix}$	$\begin{pmatrix}0.27e^{-i2.48}\\0.4e^{i1.55}\\0.4e^{-i0.27}\end{pmatrix}$	0.8	0.8	0.8
0.394	$\begin{pmatrix}0.06\\-0.08\end{pmatrix}$	$\begin{pmatrix}0.04\\0.09\end{pmatrix}$	$\begin{pmatrix}0.1\\0.01\end{pmatrix}$	$\begin{pmatrix}0.47e^{i2.78}\\0.1e^{i2.34}\\0.47e^{i1.2}\end{pmatrix}$	$\begin{pmatrix}0.38e^{i0.74}\\0.47e^{i2.44}\\0.29e^{i1.1}\end{pmatrix}$	$\begin{pmatrix}0.36e^{-i1.01}\\0.44e^{i0.85}\\0.34e^{i2.75}\end{pmatrix}$	0.9	0.9	0.9
0.485	$\begin{pmatrix}0.1\\0.08\end{pmatrix}$	$\begin{pmatrix}-0.12\\0.04\end{pmatrix}$	$\begin{pmatrix}0.02\\-0.13\end{pmatrix}$	$\begin{pmatrix}0.44e^{i1.71}\\0.46e^{i0.24}\\0.22e^{i2.38}\end{pmatrix}$	$\begin{pmatrix}0.33e^{i1.45}\\0.44e^{i2.54}\\0.4e^{-i2.5}\end{pmatrix}$	$\begin{pmatrix}0.45e^{-i1.5}\\0.17e^{i1.6}\\0.48e^{-i3.06}\end{pmatrix}$	0.92	0.92	0.92
0.579	$\begin{pmatrix}0.25\\0.1\end{pmatrix}$	$\begin{pmatrix}0.22\\-0.15\end{pmatrix}$	$\begin{pmatrix}0.02\\0.27\end{pmatrix}$	$\begin{pmatrix}0.44e^{-i2.12}\\0.28e^{i1.76}\\0.47e^{-i0.36}\end{pmatrix}$	$\begin{pmatrix}0.38e^{-i1.88}\\0.41e^{-i0.91}\\0.42e^{i0.21}\end{pmatrix}$	$\begin{pmatrix}0.39e^{-i0.62}\\0.49e^{i0.94}\\0.31e^{-i0.65}\end{pmatrix}$	0.98	0.98	0.98
0.596	$\begin{pmatrix}0.23\\0.15\end{pmatrix}$	$\begin{pmatrix}0.25\\-0.12\end{pmatrix}$	$\begin{pmatrix}0.02\\0.27\end{pmatrix}$	$\begin{pmatrix}0.48e^{-i2.78}\\0.19e^{i2.6}\\0.47e^{i1.85}\end{pmatrix}$	$\begin{pmatrix}0.48e^{-i2.53}\\0.47e^{i2.08}\\0.21e^{i-0.44}\end{pmatrix}$	$\begin{pmatrix}0.48e^{i2.77}\\0.2e^{-i2.55}\\0.47e^{-i1.85}\end{pmatrix}$	0.98	0.98	0.98
0.624	$\begin{pmatrix}0.17\\0.12\end{pmatrix}$	$\begin{pmatrix}-0.18\\0.08\end{pmatrix}$	$\begin{pmatrix}0.02\\-0.2\end{pmatrix}$	$\begin{pmatrix}0.48e^{-i1.46}\\0.32e^{-i0.1}\\0.38e^{-i2.87}\end{pmatrix}$	$\begin{pmatrix}0.35e^{-i0.31}\\0.37e^{i2.2}\\0.47e^{-i2.21}\end{pmatrix}$	$\begin{pmatrix}0.17e^{i2.2}\\0.49e^{-i2.8}\\0.46e^{i1.86}\end{pmatrix}$	0.96	0.96	0.9

Parametrization of other constituent states of the (ab,bc,ca) type phase, such as the spin configurations shown in Fig. 8, is done using the Fourier transform of the spin orders $\{\mathbf{S}_\alpha(\mathbf{q}_\mu)\}$ from MC minimization. The "purified" order is obtained by simply inverse F.T. the vectors $\{\mathbf{S}_\alpha(\mathbf{q}_\mu)\}$, given in Table VIII, using Eq. (B4):

$$\mathbf{S}^{\text{recons}}_{i(\alpha)} = \mathcal{N}_i \sum_{\mathbf{q}\in\{\mathbf{q}_\mu\}} \mathbf{S}_\alpha e^{i\mathbf{q}\cdot\mathbf{R}_i}. \tag{B4}$$

The ordering wave vectors and spins in Fourier space for the three orders in Fig. 8 are given in Table VIII.

We next turn to spin orders from the (a,b,c) phase. For *all* orders in this phase, spins on the three sublattices are defined by mutually exclusive wave vectors tracing out coplanar spirals. For *most* spin orders, the three sublattice dependent planes are mutually orthogonal. Spins are parametrized as

$$\begin{aligned}
\mathbf{S}^{\text{recons}}_{i(\alpha=1)} &= \mathbf{Re}[e^{(\mathbf{q}_1.\mathbf{R}_i+\varphi_1)}(\mathbf{e}_1 - i\mathbf{e}_2)]\\
\mathbf{S}^{\text{recons}}_{i(\alpha=2)} &= \mathbf{Re}[e^{(\mathbf{q}_2.\mathbf{R}_i+\varphi_2)}(\mathbf{e}_2 - i\mathbf{e}_3)]\\
\mathbf{S}^{\text{recons}}_{i(\alpha=3)} &= \mathbf{Re}[e^{\mathbf{q}_3.\mathbf{R}_i+\varphi_3)}(\mathbf{e}_1 - i\mathbf{e}_3)],
\end{aligned} \tag{B5}$$

where $\mathbf{e}_{1,2,3}$ form a triad of orthonormal vectors (see Table VI). For a few spin orders at $n = 0.226, 0.228$ and at $n = 0.527$

from within this phase, spins on two of the three sublattices lie in the same plane perpendicular to the plane in which spins on the third sublattice lie.

APPENDIX C: EVOLUTION OF LUTTINGER-TISZA EIGENVALUES WITH FILLING

The evolution of the Luttinger-Tisza matrix in the first B.Z. and the Fourier weights of a spin configuration from the highly symmetrical (a_1,b_1,c_1) phase is shown in Fig. 9, respectively. As the filling changes from $n = 1/3$ to $n = 0.41$, the ordering wave vector evolves smoothly from the zone corner to the zone center. At every filling, there are symmetry equivalent L.T. wave vectors which form the sixfold star of Luttinger-Tisza wave vectors.

Correspondence between the star of symmetry related L.T. wave vectors and the ordering vectors of the corresponding spin configuration can be obtained by looking at the Fourier weights of the MC minimized spin pattern at every filling. In our MC minimization, independent runs beginning from random spin configurations at "high temperatures" relax to ground states which select different sets of wave vectors from the star of L.T. wave vectors. Figure 10 shows the Fourier weights in the first Brillouin zone for a spin pattern taken from a filling at $n = 0.375$. The sharp peaks in the zone indicate that the order has a well defined wave vector content which can be detected experimentally in neutron scattering experiments.

APPENDIX D: CLASSIFICATION OF SYMMETRY BROKEN PHASES

Spin orders with the same broken symmetries in Fourier space are classified as a single phase. The phase diagram in Fig. 4 in this paper shows eight such phases, each shown in a different color. The most prominent of these phases is also listed in Table III. In this section, we take representative spin configurations from the most dominant phases in Fig. 4 in this paper and by looking at their Fourier space composition, illustrate why they form part of a smoothly connected second order phase. This section will also help to establish the nomenclature for the different phases.

We begin with the kind of phases where the dominant modes on each sublattice are made out of two of the sixfold Luttinger-Tisza stars of wave vectors. The first kind of order has different weights of the modes on the three sublattices—indicated as a (ab,bc,ca) phase. The second phase is more symmetric as can be seen in Table IV and is labeled (a_1b_2,c_1a_2,b_1c_2) indicating two distinct $\eta_\alpha(\mathbf{q})$ magnitudes across all α. A wave vector a uses one of the two η_α values denoted by subscript (1) on sublattice one and the second Fourier weight (2) on sublattice two. The same goes for the other wave vectors b,c highlighting the symmetry of the state.

The next kind of phase is where each sublattice is made out of its own independent single dominant Luttinger-Tisza wave vector. There are again two types of such phases shown in Fig. 11. One in which the Fourier weights of each of the three wave vectors a,b,c is different on each sublattice. This phase is labeled as (a,b,c). The second type of phase is a highly symmetric version of the former type. Each sublattice has the same weight of the dominant Fourier mode and is labeled (a_1,b_1,c_1). The Fourier components and weights of the spin orders from these two types of phases are enlisted in Table VII.

The next category of phases are the $1\mathbf{Q}$ type orders, where all sublattices are made out of the same dominant wave vector. These again fall into a symmetric $-(a_1,a_1,a_1)$ and an asymmetric version (a,a,a). Fourier weights of the dominant mode of spin orders from these two types of phases are shown in Table V.

APPENDIX E: STATE SELECTION IN THE PRESENCE OF A SUPEREXCHANGE INTERACTION

Here we show that the *Cuboc1* state is also selected from the family of degenerate states of the nearest neighbor HAF on kagome by turning on the KLM Hamiltonian. To this end, we add a strong nearest neighbor antiferromagnetic interaction of strength J_{ex} to the KLM Hamiltonian and using exact diagonalization explore the stability of states within the variational approach outlined before.

Figure 12 shows the phase diagram in the presence of a strong $J_{ex} = 10t$ which suppresses all the incommensurate orders and selects within the manifold of the three 120 degree

TABLE VIII. Ordering wave vectors and spin F.T. for reconstructing orders (1) at $n = 0.115$, (2) at $n = 0.146$, and (3) at $n = 0.181$ occurring in the phase diagram in Fig. 4 of this paper. From left to right: order number corresponding to labeling in Fig. 4 of this paper, ordering wave vectors $\mathbf{q}_{1,2,3}$ for the $3\mathbf{Q}(ab,bc,ca)$ state, and spin F.T. at each wave vector. An approximate and un-normalized spin order can be constructed using the information provided above using the recipe provided in the text [see Eq. (B4)].

#	$\mathbf{q}_1(2\pi)$	$\mathbf{q}_2(2\pi)$	$\mathbf{q}_3(2\pi)$	$\mathbf{S}_1(\mathbf{q}_1)$	$\mathbf{S}_1(\mathbf{q}_2)$	$\mathbf{S}_2(\mathbf{q}_2)$	$\mathbf{S}_2(\mathbf{q}_3)$	$\mathbf{S}_3(\mathbf{q}_1)$	$\mathbf{S}_3(\mathbf{q}_3)$
(1)	$\begin{pmatrix}0.19\\-0.13\end{pmatrix}$	$\begin{pmatrix}0.02\\-0.22\end{pmatrix}$	$\begin{pmatrix}0.21\\0.09\end{pmatrix}$	$\begin{pmatrix}0.33e^{i1.4}\\0.3e^{-i0.3}\\0.16e^{i3.1}\end{pmatrix}$	$\begin{pmatrix}0.32e^{-i0.8}\\0.33e^{-i2.4}\\0.11e^{i1.6}\end{pmatrix}$	$\begin{pmatrix}0.36e^{-i0.6}\\0.37e^{-i2.3}\\0.13e^{i1.7}\end{pmatrix}$	$\begin{pmatrix}0.09e^{-i2.8}\\0.15e^{-i3.1}\\0.4e^{-i3}\end{pmatrix}$	$\begin{pmatrix}0.37e^{i1.2}\\0.34e^{-i0.4}\\0.18e^{i3}\end{pmatrix}$	$\begin{pmatrix}0.09e^{i2.7}\\0.15e^{i3}\\0.4e^{-i3.1}\end{pmatrix}$
(2)	$\begin{pmatrix}0.15\\-0.1\end{pmatrix}$	$\begin{pmatrix}0.02\\-0.18\end{pmatrix}$	$\begin{pmatrix}0.17\\0.07\end{pmatrix}$	$\begin{pmatrix}0.29e^{i1.1}\\0.15e^{-i2.3}\\0.33e^{-i0.5}\end{pmatrix}$	$\begin{pmatrix}0.29e^{i1.9}\\0.15e^{-i1.5}\\0.32e^{i0.3}\end{pmatrix}$	$\begin{pmatrix}0.33e^{i2}\\0.17e^{-i1.4}\\0.37e^{i0.4}\end{pmatrix}$	$\begin{pmatrix}0.19e^{i2}\\0.39e^{2i}\\0.04e^{i2}\end{pmatrix}$	$\begin{pmatrix}0.33e^{i}\\0.16e^{-i2.4}\\0.37e^{-i0.6}\end{pmatrix}$	$\begin{pmatrix}0.19e^{i1.9}\\0.39e^{i1.9}\\0.04e^{i1.9}\end{pmatrix}$
(3)	$\begin{pmatrix}0.02\\-0.13\end{pmatrix}$	$\begin{pmatrix}-0.12\\0.05\end{pmatrix}$	$\begin{pmatrix}0.1\\0.08\end{pmatrix}$	$\begin{pmatrix}0.06e^{-i0.6}\\0.03e^{-i0.6}\\0.47e^{i2.5}\end{pmatrix}$	$\begin{pmatrix}0.29e^{i2.6}\\0.36e^{-i0.5}\\0.01e^{i2.6}\end{pmatrix}$	$\begin{pmatrix}0.36e^{-i3}\\0.29e^{-i3}\\0.06e^{-i3}\end{pmatrix}$	$\begin{pmatrix}0.06e^{-i0.5}\\0.03e^{-i0.5}\\0.46e^{i2.6}\end{pmatrix}$	$\begin{pmatrix}0.3e^{i2.5}\\0.37e^{-i0.6}\\0.01e^{i2.5}\end{pmatrix}$	$\begin{pmatrix}0.36e^{-i2.9}\\0.29e^{-i2.9}\\0.06e^{-i2.9}\end{pmatrix}$

states the $\mathbf{q} = 0$, $\sqrt{3} \times \sqrt{3}$, and the *cuboc1* order. As can be seen, large parts of the phase diagram are dominated by the *cuboc1* state. (For examples of '3Q' states, other than *cuboc1*, see Tables VI–VIII.)

[1] E. F. Shender, V. B. Cherepanov, P. C. W. Holdsworth, and A. J. Berlinsky, Phys. Rev. Lett. **70**, 3812 (1993).
[2] S. E. Palmer and J. T. Chalker, Phys. Rev. B **62**, 488 (2000).
[3] C. L. Henley, Phys. Rev. B **80**, 180401(R) (2009).
[4] U. Hizi and C. L. Henley, Phys. Rev. B **80**, 014407 (2009).
[5] G. W. Chern and R. Moessner, Phys. Rev. Lett. **110**, 077201 (2013).
[6] D. Solenov, D. Mozyrsky, and I. Martin, Phys. Rev. Lett. **108**, 096403 (2012).
[7] S. Hayami, T. Misawa, Y. Yamaji, and Y. Motome, Phys. Rev. B **89**, 085124 (2014).
[8] Y. Akagi, M. Udagawa, and Y. Motome, Phys. Rev. Lett. **108**, 096401 (2012).
[9] T. A. Kaplan and N. Menyuk, Philos. Mag. **87**, 3711 (2006).
[10] K. Ohgushi, S. Murakami, and N. Nagaosa, Phys. Rev. B **62**, R6065 (2000).
[11] M. Taillefumier, B. Canals, C. Lacroix, V. K. Dugaev, and P. Bruno, Phys. Rev. B **74**, 085105 (2006).
[12] I. Martin and C. D. Batista, Phys. Rev. Lett. **101**, 156402 (2008).
[13] Y. Akagi and Y. Motome, J. Phys. Soc. Jpn. **79**, 083711 (2010).
[14] L. Messio, B. Bernu, and C. Lhuillier, Phys. Rev. Lett. **108**, 207204 (2012).
[15] Gia-Wei Chern, Phys. Rev. Lett. **105**, 226403 (2010).
[16] K. Barros and Y. Kato, Phys. Rev. B **88**, 235101 (2013).
[17] Y. Kato, I. Martin and C. D. Batista, Phys. Rev. Lett. **105**, 266405 (2010).
[18] S. R. Sklan and C. L. Henley, Phys. Rev. B **88**, 024407 (2013); M. F. Lapa and C. L. Henley, arXiv:1210.6810.
[19] M. A. Ruderma and C. Kittel, Phys. Rev. **96**, 99 (1954).
[20] T. Kasuya, Prog. Theor. Phys. **16**, 45 (1956).
[21] K. Yosida, Phys. Rev. **106**, 893 (1957).
[22] L. Messio, C. Lhuillier, and G. Misguich, Phys. Rev. B **83**, 184401 (2011).
[23] J. M. Luttinger and L. Tisza, Phys. Rev. **70**, 954 (1946).
[24] A. Chubukov, Phys. Rev. Lett. **69**, 832 (1992).
[25] S. Hayami and Y. Motome, Phys. Rev. B **90**, 060402(R) (2014).
[26] J. C. Domenge, P. Sindzingre, C. Lhuillier, and L. Pierre, Phys. Rev. B **72**, 024433 (2005).
[27] P. W. Anderson, Phys. Rev. **100**, 675 (1955).
[28] P. G. De Gennes, Phys. Rev. **118**, 141 (1960).
[29] M. E. Zhitomirsky, Phys. Rev. B **78**, 094423 (2008).
[30] C. L. Henley and E. P. Chan, J. Magn. Magn. Mater. **140-144**, 1693 (1995).
[31] K. Barros, J. W. F. Venderbos, G. W. Chern, and C. D. Batista, Phys. Rev. B **90**, 245119 (2014).
[32] L. A. Fenner, A. A. Dee, and A. S. Wills, J. Phys. Condens. Matter **21**, 452202 (2009).
[33] W. Wu *et al.*, Europhys. Lett. **85**, 17009 (2009).